sciendo
Power Electronics and Drives
Volume 9(44), 2024 DOI: 10.2478/pead-2024-0016

Real-time Neural Sliding Mode Linearization Control for a Doubly Fed Induction Generator under Disturbances

Research paper

Larbi Djilali[a]*, Moussa Boukhnifer[b], Edgar N. Sanchez[c], Jesús A. Medrano Hermosillo[a], Abraham E. Rodríguez Mata[a]

[a]*TecNM Chihuahua, Av. Tecnologico 2909, Tecnológico, Chihuahua, México*
[b]*Université de Lorraine, LCOMS, 57000 Metz, France*
[c]*Department of Electrical Engineering, Cinvestav Guadalajara, Zapopan, Mexico*

Received: 26 January 2024; Accepted: 10 March 2024

Abstract: This paper presents an experimental implementation of a Neural Sliding Mode Linearization approach for the control of a double-fed induction generator connected to an infinite bus via transmission lines. The rotor windings are connected to the grid via a back-to-back converter, while the stator windings are directly coupled to the network. The chosen control scheme is applied to obtain the required stator power trajectories by controlling the rotor currents and to track the desired values of the DC-link output voltage and the grid power factor. This controller is based on a neural identifier trained online using an Extended Kalman Filter. Based on such identifier, an adequate model is obtained, which is used for synthesizing the required controllers. The proposed control scheme is experimentally verified on 1/4 HP DFIG prototype considering normal and abnormal grid conditions. In addition, maximum power extraction from a random wind profile is tested in the presence of different grid scenarios. Moreover, a comparison with conventional control schemes is performed. The obtained results illustrate the capability of the proposed control scheme to achieve active power, reactive power, and DC voltage desired trajectories tracking and to operate the wind power system even in the presence of parameter variation and grid disturbances, which helps to ensure the stability of the system and improve generated power quality.

Keywords: *Doubly Fed Induction Generator • Real-Time • Sliding Mode • Neural Linearization • Neural Networks • Wind Turbine*

1. Introduction

Wind power system is widely used as an alternative source for power generation [1]. For variable speed wind conversion systems, the most commonly installed electric generator is the Doubly Fed Induction Generator (DFIG) because of its advantages, such as reducing mechanical efforts, reducing the cost of inverters, and the possibility of simultaneous stator active and reactive power control [2]. The stator windings of the DFIG are directly connected to the grid, while the rotor windings are connected to the grid via a back-to-back converter. By using such a configuration, a decoupling between the mechanical speed and the grid frequency can be achieved [3]. In fact, the grid-side converter (GSC) is connected to the grid via a step-up transformer; this converter is used to feed the DFIG rotor windings via the rotor-side converter (RSC), ensuring a stable DC link output voltage [1].

For the above configuration, different control schemes have been proposed. The well known control approach for the DFIG is the Field Oriented Control (FOC), where state transformations are applied to perform linearization and decoupling [4]. In [5], an experimental implementation of the FOC technique with a Proportional-Integral (PI) controller (PI-FOC) is investigated, which is used to control the DFIG powers; voltages and currents are utilized to obtain the rotor electrical position. In [1], an hysteresis technique is proposed for the GSC, and the PI-FOC

* *Email: larbidjar@chihuahua.tecnm.mx*

scheme is included to control the RSC. Industrially, the PI-FOC approach is the preferred controller for DFIG power generation [6]. However, implementation of this controller is highly dependent on the DFIG parameters knowledge [7]. Recently, a lot of attention has been dedicated to 25 the Sliding Mode Control (SMC) because of its robustness to perturbations. It is designed to keep the controlled dynamics onto a sliding manifold [4], which is usually defined as the error of the real and the desired output behaviors. In [8], a real-time SMC for DFIG stator powers is presented. In [9], a block control SMC is developed for the DFIG stator reactive power and the electromechanical torque. The major drawbacks of conventional SMC is that in order to select the sliding manifold, the state space model is required, which does it sensitive to parameter variations; in addition, the controlled system can be destabilized by chattering [10].

On the other hand, high penetration of the WT power in medium and high voltage grids requires new grid codes in order to ensure DFIG Low-Voltage Ride-Through (LVRT) capacity [11], [12]. To improve LVRT capacity, different hardware solutions have been developed. In [13], crowbar and chopper devices are utilized to protect the DFIG and the DC-link during faults respectively. In [14], a series dynamic resistance a chopper combination is used to ensure stability of the DFIG in presence of grid disturbances. In [15], a parallel impedance crowbar and series resistance-inductance circuit are proposed to enhance the LVRT of the DFIG during faults. Authors in [16] present an enhanced corwbrless LVRT strategy for DFIG in presence of symmetric voltage dip; the proposed solution eliminate the crowbar by employing a modified PI controllers, a series resistance-inductance is inserted between the rotor widings and the RSC when the rotor currents exceed their threshold value during faults. The above solutions need extra protection devices, which increase the control scheme cost; additionally, the control objective should be modified from tracking to stability and may stop power generation during faults. In order to overcome those disadvantages, computational solutions have been developed. In [17], [18], an PI and a Proportional-Resonant (PR) controllers have been proposed to improve LVRT capacity of the DFIG. To implement them, a decomposition process is needed, which does the control strategy implementation more complex. Another work is presented in [19] where a fuzzy second order integral terminal sliding mode control is designed for the DFIG rotor and grid side converters, and a series GSC is included to avoid DFIG disconnection from the grid during fault conditions. The conventional SMC [20], [21] and the sliding mode based extended active power theory [22] are proposed to operate the DFIG in presence of grid disturbances. The obtained results illustrate their effectiveness; however, those controllers are designed using the plant physical model, which does not ensure stability of the closed-loop system with respect to unmatched perturbation and the upper bound value is required [10]. Recently, Neural Networks (NNs) can be used to approximate the DFIG and the DC-link dynamics in presence of different grid scenarios. In [23], a DFIG controller based on neural identification is investigated, where a Recurrent High Order Neural Network (RHONN) identifier based inverse optimal control is developed; this controller is experimentally validated without considering LVRT. Other work based on neural identification is published in [24], where a neural SMC associated with the FOC is selected to control a DFIG prototype under different grid scenarios; the SMC is implemented as the main controller and chattering still occur. This paper presents the development and the experimental implementation of Neural Sliding Mode Linearization (N-SM-L) controllers for the RSC and the GSC of a DFIG prototype connected to an infinity bus through a transmission line. Regarding the high penetration of wind power systems into main grids, big efforts have been made to ensure uninterrupted power generation during faults. To achieve such, the proposed control schemes should ensure a constant DC-link voltage, and better value of the power factor, and improved active and reactive power even in the presence of grid faults. The main contributions of this paper are: 1) by using a neural identifier, adequate models under different grid conditions are obtained. The neural models are used to design linearization controllers which are the main components on the proposed scheme. These controllers help to obtain a decoupled linearization of the system and to reject disturbances caused by fault grid conditions and/or parameter variations. 2) a discrete-time SMC, which is considered as a secondary one, is proposed to ensure the desired references tracking and to reject the neural identification errors which are very small as addressed in [25]. As results, small sliding mode control gains are required reflecting a large reduction in chattering. 3) robustness to grid disturbances is experimentally evaluated illustrating the proposed controllers performances, and their capability to improve LVRT in order to keep power generation in presence of different types of grid disturbances. 4) additionally, the proposed technique is adapted to improve the generated active power from the wind using Maximum Point Power Tracking (MPPT). The contents of this paper are: Section 2 presents mathematical preliminaries. In section 3, the DFIG and DClink models are briefly explained. The proposed neural identifiers for both the DFIG and DC-link are introduced in section 4. The proposed control approach is synthesized in section 5. In section 7, a real-time implementation is described and the obtained results are discussed.

2. Mathematical Preliminaries

2.1. Neural Identifier

Let us consider the following non-linear system [4]

$$\begin{aligned} x_{k+1} &= f(x_k) + g(x_k)u_k \\ y_k &= h(x_k) \end{aligned} \tag{1}$$

with $x_k \in R^n$ the state space variables, $u_k \in R^m$ the control input, $y_k \in R^m$ the output to be controlled, $f(x_k)$, $g(x_k)$ and $h(x_k)$ continuous functions. Using a series-parallel structure, this state space (1) is estimated by an RHONN identifier as [26]

$$\chi_{i,k+1} = w_i^T \phi_i(x_k) + \varpi_i^T \varphi_i(x_k, u_k) \tag{2}$$

with $\chi_{i,k}$ the estimated state space, $w_i \in \Re^{Li}$ the adjustable NNs weights, ϖ_i the fixed ones, $\phi_i \in \Re^{Li}$ a smooth vector function defined as follows $\phi_i(.) = [\phi_{i,1}(.),...,\phi_{i,L}(.)]^T \in \Re^{Li}$ and L_i the connection number, such as each component is given as $\phi_{ij}(.) = \phi_{i,1}(S(x_{1,k}),...,S(x_{n,k}))^T$, ϕ_i the inputs function depends to the system structure. $S(.)$ is the hyperbolic tangent function. The Extended Kalman Filter (EKF) algorithm is used to train the selected RHONN identifier [25]. It is expressed by [25]

$$e_{i,k} = x_{i,k} - \chi_{i,k} \tag{3}$$

$$w_{i,k+1} = w_{i,k} + \eta_i K_{i,k} e_{i,k} \tag{4}$$

$$P_{i,k+1} = P_{i,k} - K_{i,k} H_{i,k}^T P_{i,k} + Q_{i,k} \tag{5}$$

$$K_{i,k} = P_{i,k} H_{i,k} \left[R_{i,k} + H_{i,k}^T P_{i,k} H_{i,k} \right]^{-1} \tag{6}$$

$$H_{ij,k} = \left[\frac{\partial \chi_{i,k}}{\partial w_{ij,k}} \right]^T_{w_{i,k}=w_{i,k+1}} \tag{7}$$

where $e_i \in R$ is the error between the real state vector and the estimated one, $P_i \in R^{Li \times Li}$ is the covariance matrix of predicted error, L_i is the neural identifier weights, η_i is an EKF design parameter, $K_{i,k} \in R^{Li \times m}$ is the Kalman gain matrix, $R_{i,k} \in R^{m \times m}$ and $Q_{i,k} \in R^{Li \times Li}$ are the measurement noise associated covariance matrices and the respective state one, $H_i \in R^{Li \times m}$ is the derivative of each neural identifier state with respect to the weights.

3. System Modeling

Figure 1 shows the DFIG configuration, with a back-to-back converter based on Insulated-Gate Bipolar Transistors (IGBT) inserted to connect the DFIG rotor to the grid, whereas the stator is directly linked to the grid.

3.1. DFIG

The DFIG discrete-time model on the $d-q$ frame is [9]

$$i_{sd,k+1} = i_{sd,k} + t_s(-a_1 i_{sd,k} + (w_s + a_2 w_{r,k}) i_{sq,k} - b_1 u_{rd,k} + \Upsilon_{1,k}) \tag{8}$$

$$i_{sq,k+1} = i_{sq,k} + t_s(-(w_s + a_2 w_{r,k}) i_{sd,k} - a_1 i_{sq,k} - b_1 u_{rq,k} + \Upsilon_{2,k}) \tag{9}$$

$$i_{rd,k+1} = i_{rd,k} + t_s((-a_8 w_s + a_9) i_{rq,k} - a_7 i_{rd,k} + b_2 u_{rd,k} + \Upsilon_{3,k}) \tag{10}$$

$$i_{rq,k+1} = i_{rq,k} + t_s((a_8 w_s - a_9) i_{rd,k} - a_7 i_{rq,k} + b_2 u_{rq,k} + \Upsilon_{4,k}) \tag{11}$$

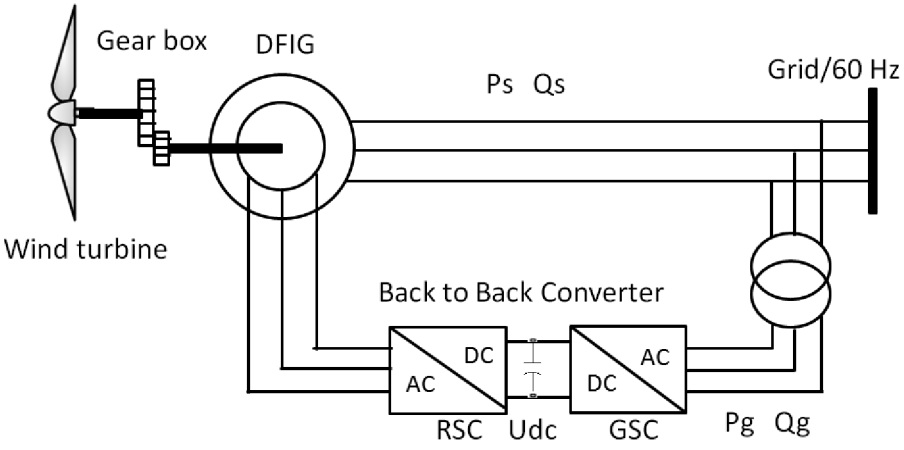

Figure 1. DFIG connected to the electrical grid.

with $\Upsilon_{1,k} = a_3 i_{rd,k} + a_4 i_{rq,k} + d_1 u_{sd,k}$, $\Upsilon_{2,k} = a_3 i_{rq,k} - a_4 a_9 i_{rd,k} + d_1 u_{sq,k}$ the DFIG stator interconnecting terms, $\Upsilon_{3,k} = a_5 i_{sd,k} + a_6 a_9 i_{sq,k} - d_2 u_{sd,k}$, $\Upsilon_{4,k} = -a_6 a_9 i_{sd,k} + a_5 i_{sq,k} - d_2 u_{sq,k}$ the DFIG rotor interconnecting terms, where $a_1 = \frac{R_s}{\sigma L_s}, a_2 = \frac{L_m^2}{\sigma L_s L_r}, a_3 = \frac{R_r L_m}{\sigma L_s L_r}, a_4 = \frac{L_m}{\sigma L_s}, a_5 = \frac{R_s L_m}{\sigma L_s L_r}$, $a_6 = \frac{L_m}{\sigma L_r}$, $a_7 = \frac{R_r}{\sigma L_r}$, $a_8 = \frac{L_m^2}{\sigma L_s L_r}$, $a_9 = \frac{1}{\sigma} w_{r,k}, d_1 = \frac{1}{\sigma L_s}, d_2 = \frac{L_m}{\sigma L_s L_r}, b_1 = \frac{L_m}{\sigma L_s L_r}, b_2 = \frac{1}{\sigma L_r}$, with ω_r, ω_s the rotor and stator electrical speed, L_r and L_s the rotor and stator inductances respectively, L_m the stator and rotor mutual inductance, R_r, R_s the resistance of the rotor and the stator, t_s the sample time.

3.2. DC-link

The DC-link discrete-time model on the $d-q$ frame is [9]

$$U_{dc,k+1} = U_{dc,k} + t_s \frac{3}{2CU_{dc,k}} \left(u_{gd,k} i_{gd,k} + \Upsilon_{5,k}\right) \tag{12}$$

$$i_{gd,k+1} = i_{gd,k} - t_s \left(\frac{R_g}{L_g} i_{gd,k} + \frac{1}{L_g} u_{gcd,k} - \Upsilon_{6,k}\right) \tag{13}$$

$$i_{gq,k+1} = i_{gq,k} - t_s \left(\frac{R_g}{L_g} i_{gq,k} + \frac{1}{L_g} u_{gcq,k} - \Upsilon_{7,k}\right) \tag{14}$$

where $\Upsilon_{5,k} = u_{gq,k} i_{gq,k}$, $\Upsilon_{6,k} = -w_s i_{gq,k} - \frac{1}{L_g} u_{gd,k}$, $\Upsilon_{7,k} = w_s i_{gd,k} - \frac{1}{L_g} u_{gq,k}$ are the DC-link interconnection terms, i_{gq} and i_{gd} are the grid currents, $u_{gcd,k}$ and $u_{gcq,k}$ are the GSC $d-q$ voltages considered as the control vector, $u_{gd,k}$ and $u_{gq,k}$ are the grid $d-q$ voltages, L_g is the grid inductances of (H), R_g is the grid resistances (Ω), C is the capacitor of DC-link (F).

By using the discrete-time separation principle [27], the synthesis of N-SM-L controller is done without including the neural identifier and vice versa [25], [27].

4. Neural Identifier

In order to select the RHONN identifier, the following considerations are taken into account

- **C1.** The selected RHONN identifier structure is mainly based on the plant mathematical model.
- **C2.** The selected neural identifier should be implemented using the minimum possible number of sensors to reduce cost.
- **C3.** Taking into account neural identification properties such as its capability to absorb disturbances [25], the interconnection terms on (8) (14) are considered as disturbances.

4.1. Neural DFIG Model

The RHONN model for the DFIG stator and rotor currents is given as

$$\hat{i}_{sd,k+1} = w_{11,k}S(i_{sd,k}) + w_{12,k}S(i_{sq,k}) + w_{13,k}S(i_{sd,k})S(i_{sq,k}) + \varpi_1 u_{rd,k} \quad (15)$$

$$\hat{i}_{sq,k+1} = w_{21,k}S(i_{sd,k}) + w_{22,k}S(i_{sq,k}) + w_{23,k}S(i_{sq,k})S(i_{sd,k}) + \varpi_2 u_{rq,k} \quad (16)$$

$$\hat{i}_{rd,k+1} = w_{31,k}S(i_{rd,k}) + w_{32,k}S(i_{rq,k}) + w_{33,k}S(i_{rd,k})S(i_{rq,k}) + \varpi_3 u_{rd,k} \quad (17)$$

$$\hat{i}_{rq,k+1} = w_{41,k}S(i_{rq,k}) + w_{42,k}S(i_{rd,k}) + w_{43,k}S(i_{rd,k})S(i_{rq,k}) + \varpi_4 u_{rq,k} \quad (18)$$

where $\hat{i}_{sq,k}$, $\hat{i}_{sd,k}$, $\hat{i}_{rd,k}$ and $\hat{i}_{rq,k}$ are the estimate dynamics of $i_{sd,k}$, $i_{sd,k}$, $i_{rd,k}$ and $i_{rq,k}$, w_{ij} are the adaptive neural identifier weights, and ϖ_i are the fixed ones.

4.2. Neural DC-link Model

The DC-link RHONN identifier is selected as

$$\hat{U}_{dc,k+1} = w_{51}S(U_{dc,k}) + w_{52})S(i_{gq,k})S(U_{dc,k} + \varpi_5 i_{gd,k} \quad (19)$$

$$\hat{i}_{gd,k+1} = w_{61}S(i_{gd,k}) + w_{62}S(i_{gq,k}) + w_{63}S(U_{dc,k}) + \varpi_6 u_{gcd,k} \quad (20)$$

$$\hat{i}_{gq,k+1} = w_{71}S(i_{gq,k}) + w_{72}S(i_{gd,k}) + +\varpi_7 u_{gcq,k} \quad (21)$$

where $U_{dc,k}$, $i_{gd,k}$, and $i_{gq,k}$ are the DC-link real state vector, $\hat{U}_{dc,k}$, $\hat{i}_{gd,k}$, and $\hat{i}_{gq,k}$ are the estimate one.

5. Controllers Synthesis

The proposed structure is divided into: The RSC controller and the GSC one. The respective scheme for both controllers is displayed in Figure 2. The DFIG and the DC link mathematics model are considered unknown, the RHONN identifier is used to approximate online their models. The EKF is used to 165 minimize the error between the real state vector $x_{i,k}$ and the estimated one $\chi_{i,k}$ by adjusting neural wights $\omega_{i,k}$. This online identification helps to approximate the mathematical models of the DFIG and the DC-link even in the presence of parameter variations and/or grid disturbances. In addition, the N-SM-L controller is synthesized based on the neural model, which allows the neural linearization part of the proposed control scheme to compensate the nonlinear part of the system and helps the SM control part to achieve trajectory tracking.

5.1. Rotor Side Controller

The proposed N-SM-L control objective is to track the desired trajectories of the $i_{rd,k}$ and $i_{rq,k}$ rotor currents and to assure robustness for parameter variations and/or disturbances. Then, the output to be controlled is the DFIG rotor currents $\hat{y}_{1,k} = [\hat{h}_{11,k}\ \hat{h}_{12,k}]^T = [\hat{i}_{rd,k}\ \hat{i}_{rq,k}]^T$, and $x_{1,k} = [i_{rd,k}\ i_{rq,k}]^T$ is the real rotor currents dynamics. The expression of the output $\hat{y}_{2,k}$ at k + 1 is given as

$$\hat{y}_{1,k+1} = \begin{bmatrix} \hat{i}_{rd,k+1} \\ \hat{i}_{rq,k+1} \end{bmatrix} \quad (22)$$

Substituting (17) and (18) in (22), we obtain

$$\begin{bmatrix} \hat{i}_{rd,k+1} \\ \hat{i}_{rq,k+1} \end{bmatrix} = \begin{bmatrix} \hat{f}_{13}(x_{1,k}) \\ \hat{f}_{14}(x_{1,k}) \end{bmatrix} + D_1 \begin{bmatrix} u_{rd,k} \\ u_{rq,k} \end{bmatrix} \quad (23)$$

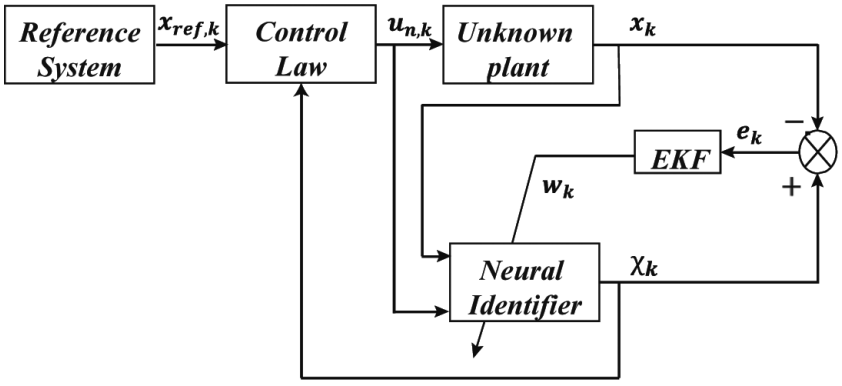

Figure 2. N-SM-L control scheme.

with $D_1 = \begin{bmatrix} \varpi_3 & 0 \\ 0 & \varpi_4 \end{bmatrix}$, and

$$\hat{f}_{13}(x_{1,k}) = w_{31,k}S(i_{rd,k}) + w_{32,k}S(i_{rq,k}) + w_{33,k}S(i_{rd,k})S(i_{rq,k})$$
$$\hat{f}_{14}(x_{1,k}) = w_{41,k}S(i_{rq,k}) + w_{42,k}S(i_{rd,k}) + w_{43,k}S(i_{rd,k})S(i_{rq,k})$$

Applying neural linearization, then the control law of the rotor currents is obtained as

$$\begin{bmatrix} u_{rd,k} \\ u_{rq,k} \end{bmatrix} = D_1^{-1} \begin{bmatrix} -\hat{f}_{13}(x_{1,k}) + v_{1,k} \\ -\hat{f}_{14}(x_{1,k}) + v_{2,k} \end{bmatrix} \tag{24}$$

where $v_{1,k}$, $v_{2,k}$ are additional linear control inputs. Substituting (24) in (17) and (18), we obtain

$$\hat{i}_{rd,k+1} = v_{1,k} \tag{25}$$

$$\hat{i}_{rq,k+1} = v_{2,k} \tag{26}$$

A discrete-time SMC is proposed to calculate $v_{1,k}$, $v_{2,k}$. The sliding manifold is given as $S_{1,k} = \begin{bmatrix} i_{rdqref,k} - \hat{i}_{rd}(k) \\ i_{rqref,k} - \hat{i}_{rq}(k) \end{bmatrix}$, whose expression at ($k$ + 1) is

$$S_{1,k+1} = \begin{bmatrix} i_{rdref,k+1} - v_{1,k} \\ i_{rqref,k+1} - v_{2,k} \end{bmatrix} \tag{27}$$

with $i_{rdqref,k}$ and $i_{rqref,k}$ the rotor $d-q$ currents references. The equivalent control $[u_{eq1,k}\, u_{eq2,k}]^T$ is calculated by

$$\begin{bmatrix} u_{eq1,k} \\ u_{eq1,k} \end{bmatrix} = \begin{bmatrix} i_{rdref,k+1} \\ i_{rqref,k+1} \end{bmatrix} \tag{28}$$

The stabilizing terms $[u_{n1,k}\, u_{n2,k}]^T$ are defined as

$$\begin{bmatrix} u_{n1,k} \\ u_{n2,k} \end{bmatrix} = -K_1 S_{1,k} \tag{29}$$

with $K_1 = [k_1\ 0;\ k_2\ 0]$ a Schur matrix, and a discrete-time SMC [4] is defined as

$$v_{1,k} = \begin{cases} u_{c1,k} & \text{if} \quad ||u_{eq1,k}|| < u_{01} \\ u_{01}\frac{u_{eq1,k}}{||u_{eq1,k}||} & \text{if} \quad ||u_{eq1,k}|| \geq u_{01} \end{cases} \tag{30}$$

where u_{01} is the control bound and $u_{c1,k} = u_{eq1,k} + u_{n1,k}$,

$$v_{2,k} = \begin{cases} u_{c2,k} & \text{if} \quad ||u_{eq2,k}|| < u_{02} \\ u_{02}\frac{u_{eq2,k}}{||u_{eq2,k}||} & \text{if} \quad ||u_{eq2,k}|| \geq u_{02} \end{cases} \tag{31}$$

with u_{02} the control bound and $u_{c2,k} = u_{eq2,k} + u_{n2,k}$. The rotor currents references are determined as [1], [20]

$$i_{rqref,k} = -\frac{P_{sref,k}L_s}{u_s L_m} \tag{32}$$

$$i_{rdref,k} = -\frac{Q_{sref,k}L_s}{u_s L_m} + \frac{u_s}{w_s L_m} \tag{33}$$

with u_s the stator voltage maximum value, $P_{sref,k}$ and $Q_{sref,k}$ the stator active and reactive power references.

5.2. Grid Side Controller

The N-SM-L control objective is to track the desired value $U_{dcref,k}$ for the DC voltage $U_{dc,k}$, and to keep the power factor f_g at the unit value. Then, the variables to be controlled are $\hat{y}_2 = [\hat{h}_{21,k}\ \hat{h}_{22,k}\ \hat{h}_{23,k}]^T = [\hat{U}_{dc,k}\ \hat{i}_{gd,k}\ \hat{i}_{gq,k}]^T$, with $x_{2,k} = [U_{dc,k}\ i_{gd,k}\ i_{gq,k}]^T$ the real DC-link dynamics. The output expression $\hat{h}_{21,k}$ at the step $k + 1$ is calculated as

$$\hat{h}_{21,k+1} = \hat{U}_{dc,k+1} = \hat{f}_{21}(x_{2,k}) + \varpi_5 i_{gd,k} \tag{34}$$

with $\hat{f}_{21}(x_{2,k}) = w_{51}S(U_{dc,k}) + w_{52}S(U_{dc,k})S(i_{gq,k})$. For control synthesis, first the neural linearization is carried out using (34); hence, the linearizing control law becomes

$$i_{gd,k} = \frac{1}{\varpi_5}\left(-\hat{f}_{21}(x_{2,k}) + v_{3,k}\right) \tag{35}$$

Substituting (35) in (19), we obtain the linearized model as

$$\hat{U}_{dc,k+1} = v_{3,k} \tag{36}$$

To calculate $v_{3,k}$, a discrete-time SMC [4] is selected such that the sliding surface is $S_{2,k} = U_{dcref,k} - \hat{U}_{dc,k}$, and $u_{eqk3,k}$ is determined using $S_{2,k+1}$ as

$$u_{eq3,k} = U_{dcref,k+1} \tag{37}$$

and, the stabilizing term $u_{n3,k}$ is defined by

$$u_{n3,k} = -k_3 S_{2,k} \tag{38}$$

with $-1 < k_3 < 1$. The desired values of the grid $i_{dg,k}$ current are determined from the DC voltage control law given in (35).

To calculate the grid $i_{qg,k}$ current desired value, the following expression is used [9]

$$i_{gqref,k} = -i_{gd,k}\frac{\sqrt{1-f_{gref}^2}}{f_{gref}} \tag{39}$$

Along the same steps as in (22)-(29), the grid currents neural linearization control law is obtained as

$$\begin{bmatrix} u_{gcd,k} \\ u_{gcq,k} \end{bmatrix} = D_2^{-1}\begin{bmatrix} -\hat{f}_{22}(x_{2,k}) + v_{4,k} \\ -\hat{f}_{23}(x_{2,k}) + v_{5,k} \end{bmatrix} \tag{40}$$

with $D_2 = \begin{bmatrix} \varpi_6 & 0 \\ 0 & \varpi_7 \end{bmatrix}$, and

$$\begin{aligned} \hat{f}_{22}(x_{2,k}) &= w_{61}S(i_{gd,k}) + w_{62}S(i_{gq,k}) + w_{63}S(U_{dc,k}) \\ \hat{f}_{23}(x_{2,k}) &= w_{61}S(i_{gq,k}) + w_{62}S(i_{gd,k}) \end{aligned}$$

where $v_{4,k}$, $v_{5,k}$ are decoupled linear control inputs defined by using the discretetime SMC as given in (30). The sliding surface is selected as $S_{3,k} = \begin{bmatrix} i_{gdref,k} - \hat{i}_{gd,k} \\ i_{gqref,k} - \hat{i}_{gq,k} \end{bmatrix}$ with $i_{gdref,k}$ and $i_{gqref,k}$ the grid d–q currents references. The equivalent control inputs $[u_{eq4,k}\, u_{eq5,k}]^T$ are given by

$$\begin{bmatrix} u_{eq4,k} \\ u_{eq5,k} \end{bmatrix} = \begin{bmatrix} i_{gdref,k+1} \\ i_{gqref,k+1} \end{bmatrix} \tag{41}$$

The stabilizing terms $[u_{n4,k}\, u_{n5,k}]^T$ are defined as

$$\begin{bmatrix} u_{n4,k} \\ u_{n5,k} \end{bmatrix} = -K_2 S_{3,k} \tag{42}$$

with $K_2 = [k_4\ 0; k_5\ 0]$ a Schur matrix. The respective convergence proof of the proposed controllers is presented in the Appendix.

6. Simulation Results

This section discusses the comparison study between the developed control scheme and the previous published ones, which are the PI-FOC, the classical SM-FOC, and the SM–H_∞ as experimented in [5], [20], and [28], respectively. All the compared controllers are implemented using SimPower tools of Matlab[1]. The objective is to evaluate the performance of the proposed controller and illustrate its potential compared with the other methodologies, considering timevarying trajectory tracking, robustness to parameter variations, and sensitivity to speed changing.

6.1. Tracking Test

To demonstrate the ability of the proposed scheme for trajectory tracking, the DFIG stator active power is forced to follow time-varying dynamics, while the reactive power is fixed constant. In addition, the mechanical speed and the DFIG parameters are kept at their nominal rates. Table 1 illustrates the Mean Square Error (MSE) and

1 Matlab,Simulink. de 1994-2022, ©The Math Works, Inc.

the Standard Deviation (STD) numerical results for this experiment. This test demonstrates that the proposed (N-SM-L) controller has better tracking performance in the presence of trajectory variations compared with the other controllers.

6.2. Robustness Test

In this part, the objective is to examine the developed control methodology robustness in the presence of parameter variations. It is worth noting that the stator active and reactive power references are selected as time-varying dynamics and the nominal mechanical speed is considered for this test. The MSE and STD results for the active power reference tracking are presented in Table 2.

Numerical results show that parameter variations have a significant impact on the stator active and reactive power tracking controlled by the PI-FOC, the classical SM-FOC, and the SM−H_∞, while an adequate robustness is presented in the presence of these disturbances by implementing the proposed N-SM-L controller.

6.3. Speed Changing Test

For this experiment, the objective is to examine the effects of the speed fluctuations on the DFIG-generated powers. To do such, the parameters of the DFIG are maintained at their nominal values and the generated powers are forced to track constant dynamics. However, a variable speed profile is applied for the DFIG rotor including sub-synchronous and super-synchronous speeds. Table 3 presents the MSE and the STD regarding this test. The obtained numerical results show that speed-changing significantly affect the DFIG stator generated powers as controlled by the conventional schemes, whereas this effect is largely reduced by implementing the proposed N-SM-L controller.

From the obtained results, it is very clear that the proposed N-SM-L controller has better performance regarding trajectories tracking and faults model thanks to the proposed neural identifier, which helps to approximate the DFIG model under fault conditions. In addition, based on the neural identifier, an exact feedback linearization controller, as part of the N-SM-L is obtained, which helps the control law to remove the effects of the disturbances and to ensure its stability.

Table 1. Tracking statistic results: MSE and STD.

Controller	Tracking		Controller	Tracking	
PI-FOC (P_s)	MSE STD	0.3732 0.6063	PI-FOC (Q_s)	MSE STD	0.052 0.2363
SM-FOC (P_s)	MSE STD	0.1575 0.2263	SM-FOC (Q_s)	MSE STD	0.0139 0.3835
SM−H_∞ (P_s)	MSE STD	0.422 0.1352	SM−H_∞ (Q_s)	MSE STD	0.0205 0.3624
N-SM-L (P_s)	MSE STD	$1.055e-4$ 0.0107	N-SM-L (Q_s)	MSE STD	$0.616e-4$ 0.0086

Table 2. Robustness MSE and STD values.

Controller		Parameters			
	-	R_s(200%)	L_s(100%)	L_r(100%)	L_m(90%)
PI-FOC (P_s)	MSE STD	0.3387 0.5784	0.1159 0.3406	1.5371 1.2394	0.2637 0.5142
SM-FOC (P_s)	MSE STD	0.1717 0.4420	0.0709 0.2610	0.1076 0.2430	0.1554 0.3572
SM−H_∞ (P_s)	MSE STD	0.0715 0.3451	0.0512 0.1215	0.1052 0.1723	0.1004 0.1250
N-SM-L (P_s)	MSE STD	$1.026e-4$ 0.0032	$1.84e-5$ 0.0097	$1.62e-5$ 0.0057	$1.57e-5$ 0.0247

Table 3. Tracking performances: STD and MSE.

Controller	Tracking		Controller	Tracking	
PI-FOC (P_s)	MSE STD	0.4077 0.6400	PI-FOC (Q_s)	MSE STD	0.4147 0.6367
SM-FOC (P_s)	MSE STD	0.3180 0.4671	SM-FOC (Q_s)	MSE STD	0.0126 0.0970
SM$-H_\infty$ (P_s)	MSE STD	0.3580 0.3625	SM$-H_\infty$ (Q_s)	MSE STD	0.3497 0.0920
N-SM-L (P_s)	MSE STD	$2.32e-4$ 0.0304	N-SM-L (Q_s)	MSE STD	$1.21e-4$ 0.0173

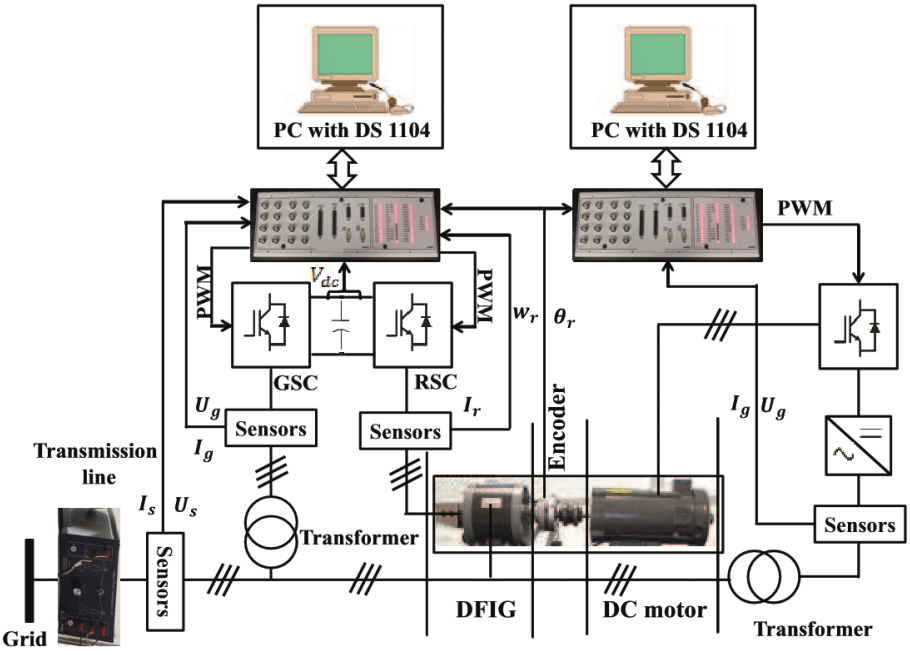

Figure 3. DFIG prototype scheme.

7. Experimental Implementation

The proposed control scheme is evaluated under normal and abnormal grid conditions. In addition, a comparison with the conventional SM-FOC is presented under grid fault conditions. The main objectives of the proposed control scheme are 1- to maintain the DC voltage constant and to reduce the voltage ripples at the DC link, which can help to improve the quality of the grid active power. 2- to maintain the nominal value of the power factor to achieve the control of the grid reactive power. 3- To track desired values of the active power obtained from the MPPT algorithm, which can ensure maximum power production. 4- To control the generated active power, which allows to maintain the value of the stator power factor desired value. It is worth noting that 1 and 2 are achieved by the GSC controller; 3 and 4 are realized by the RSC controller.

7.1. Prototype Descritption

The proposed N-SM-L control laws are tested on a DFIG prototype installed at Cinvestav- Guadalajara campus, Mexico. Figure 3 displays the experimental control scheme, which is composed of: 1) a DFIG of Lab-Volt2. 2) a DC motor3, which is coupled with the rotor shaft of the DFIG and is used to emulate a small-scale wind turbine (three-blades rotor, fixed pitch, 1.15m diameter), [29]. 3) a back-to-back converter inserted between the network and the

2 1/4 HP DFIG, Lab-Volt, Series no. 8231−00, Lab-Volt Ltda, Canada.
3 3/4 HP motor of Baldor Electric Company, P.O. Box 2400 Fort Smith, Arkansas, USA.

Table 4. System parameters

Meanings	Units	Meanings	Units
Nominal speed	1800*r/min*	Moment of Inertia	0.23*sec*
Turbine radius	1.15*m*	Stator Inductance	0.5008*H*
Nominal Power	185*V A*	Stator Resistance	0.1609Ω
Grid Inductance	0.0045*H*	Rotor Inductance	0.5008*H*
Grid Resistance	0.0014*H*	Rotor Resistance	0.0502Ω
DC Link Capacitor	0.0022*F*	Mutual Inductance	0.4775*H*

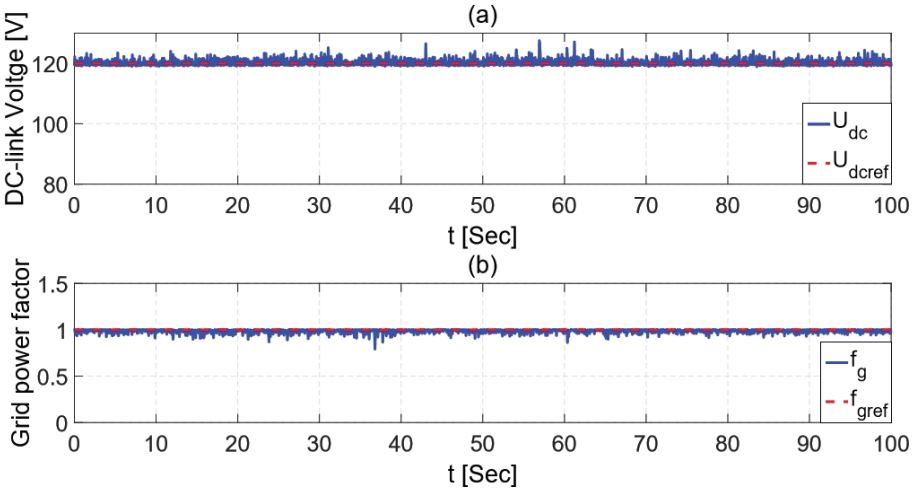

Figure 4. The behaviors of the DC-link voltage and the power factor.

DFIG rotor. 4) a transmission line module of Lab-Volt4. 5) a Personal Computer (PC) used to manage the obtained data; it is provided with two dSPACE boards *DS*11045[5] and MatLab/ Simulink[6]. In addition, electric protection circuits are installed.

Measurements of currents, voltages, and mechanical speed are obtained using the respective sensors and the DS1104 board. Space-vector pulse Width Modulation is implemented to determine commutation for both converters, which are calculated by the DS1104 Board control blocks. Table 4 illustrates the DFIG prototype nominal parameters.

7.2. GSC Controller

Figure 4-(a), (b) illustrates the controlled dynamics using the GSC, for the DC- link voltage U_{dc} and the step-up transformer power factor f_g. It is clear that such controller achieves the desired goals: a DC-link voltage of 120*V* and grid power factor equal to 1. Figure 5 - (a) presents the grid active (P_g, blue, 100*W*) and reactive powers (Q_g, red, 0*V ar*). The grid currents i_{gd}, i_{gq} dynamics are presented in Figure 5 - (b) (blue, 1.5*A* - red, 0*A*) respectively. Note that: 1) the DC voltage desired value is selected for providing enough active power to the RSC controller. 2) the unit value of the grid power factor helps to improve the quality of the supplied power to the RSC and allows to maintain the desired value of the grid reactive power, which has a large effect on the security of the WT power systems because it affects the voltage throughout the system.

7.3. RSC Controller

To test the proposed scheme capabilities, a time-varying wind speed profile is applied and the WT emulator is operated to extract the maximum available power by means a MPPT algorithm. We note that:1) the DC motor is utilized to emulate the mechanical speed such that the desired DFIG rotor shaft speed profile is applied as a

4 Transmission line of Lab-Volt Series no. 8329−00, Lab-Volt Ltda, Canada.
5 dSPACE GmbH Technologiepark 25, Paderborn, Germany. [6]Matlab,Simulink, © 1994-2019 The MathWorks, Inc.

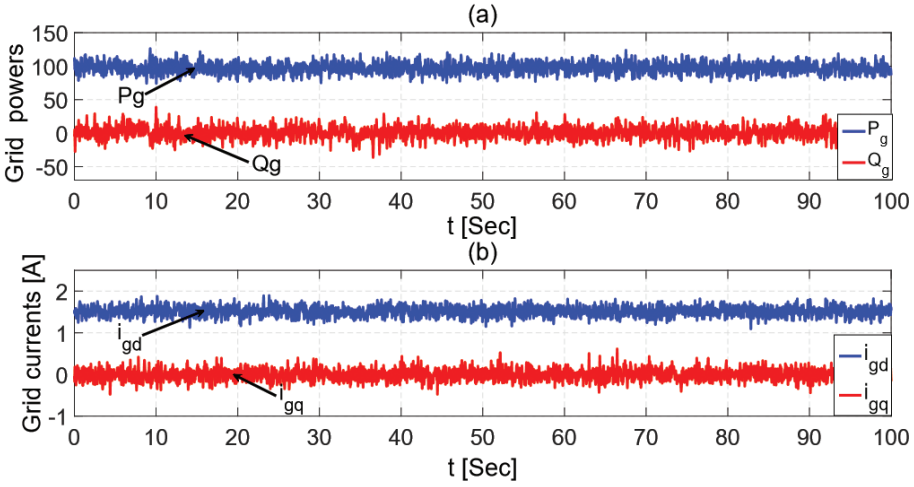

Figure 5. The behaviors of grid dynamics.

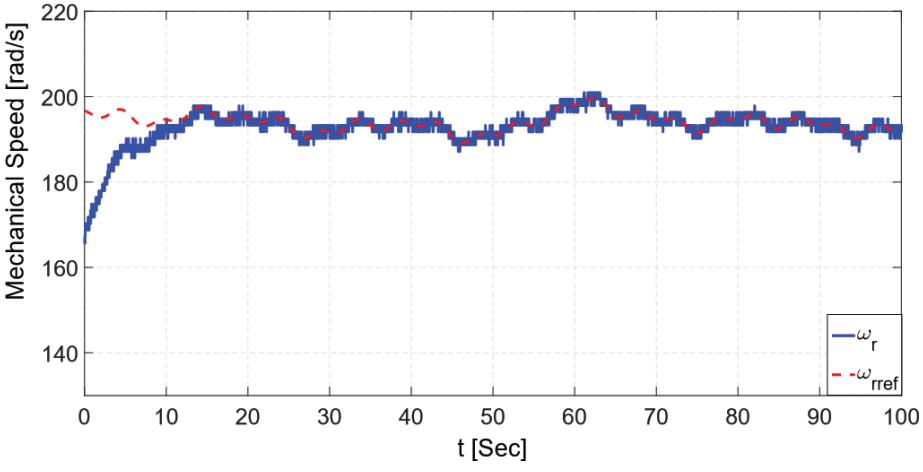

Figure 6. Variable wind Turbine Speed.

reference speed for the DC motor (0 to 2500 r/min). 2) the power factor and the DC-link voltage are kept at constant values. To improve the generated power, MPPT algorithm is applied to define the stator active power desired value as in [24]. Where, the stator active power reference is calculated using the Maximum Power Point Tracking (MPPT) algorithm based on the following equation

$$P_{ref} = K_{opt}\Omega_{mec}^{3} \tag{43}$$

with $K_{opt} = \frac{C_{pmax}(\lambda_{opt},\beta_{opt})}{\lambda_{opt}^{3}} \frac{\rho.\pi.r^{5}}{2G^{3}}$, and C_{pmax} represents the maximum yield aerodynamics of the WT, β_{opt} is the optimal angle blade, λ_{opt} is optimal relative speed. The mechanical speed behavior is presented in Figure 6. The DFIG currents rotor tracking behaviors are displayed in Figure 7; the desired trajectory for 325 the DFIG rotor $-q-$ current is also defined from the MPPT active power, and the rotor $-d-$ current is kept at a constant value calculated from reactive power desired trajectory using (32) and (33) respectively. Figure 8 and 9 presents the DFIG stator powers and currents respectively. The obtained results illustrate the capabilities of the rotor side controller for tacking the required trajectory of the active power, which improves quality of the generated power. In addition, the DFIG reactive power is kept constant at a required value, which ensures a desired power factor for the stator side. Figure 10 displays the DFIG power factor and the electromagnetic torque dynamics. From these results, variations in the mechanical speed has no significant effects on the DFIG stator active and reactive power controller. In addition, decoupling between the control axes and stability are ensured.

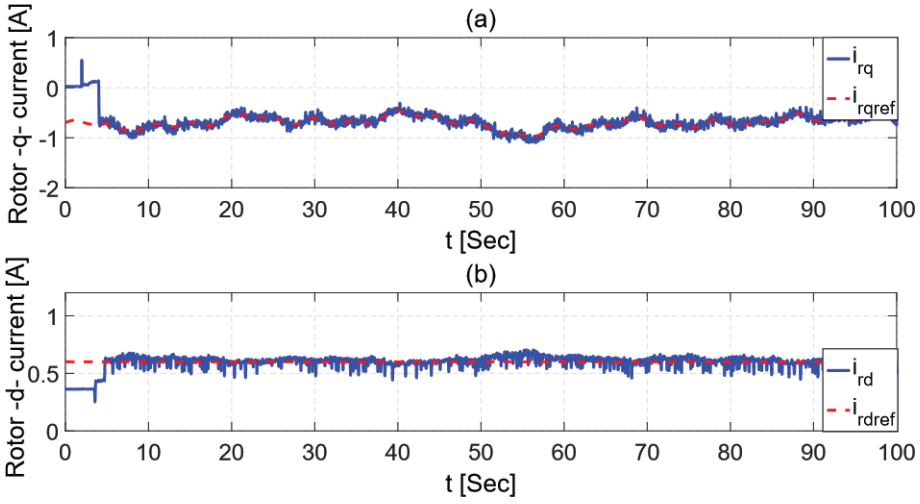

Figure 7. Rotor currents tracking.

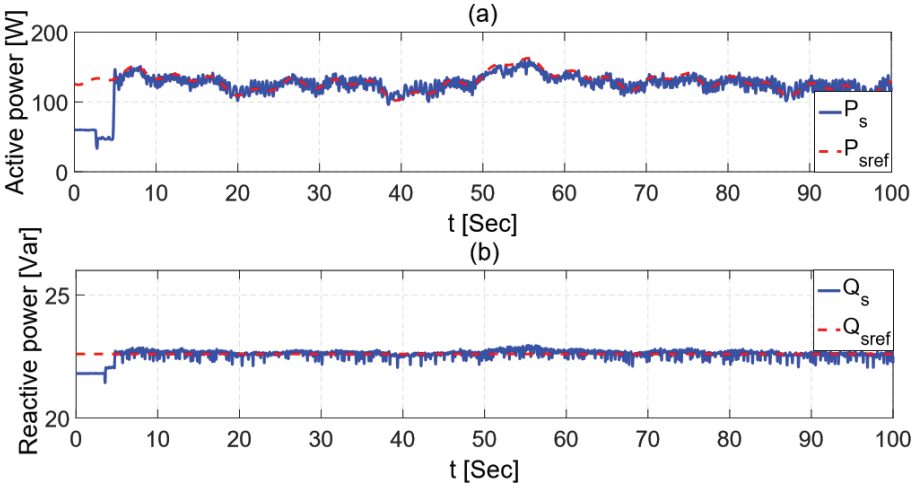

Figure 8. DFIG powers tracking.

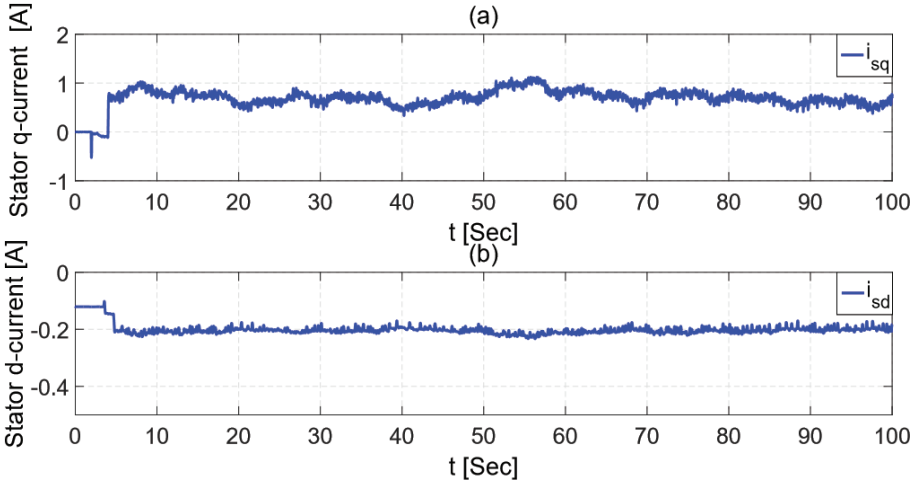

Figure 9. DFIG stator currents dynamics.

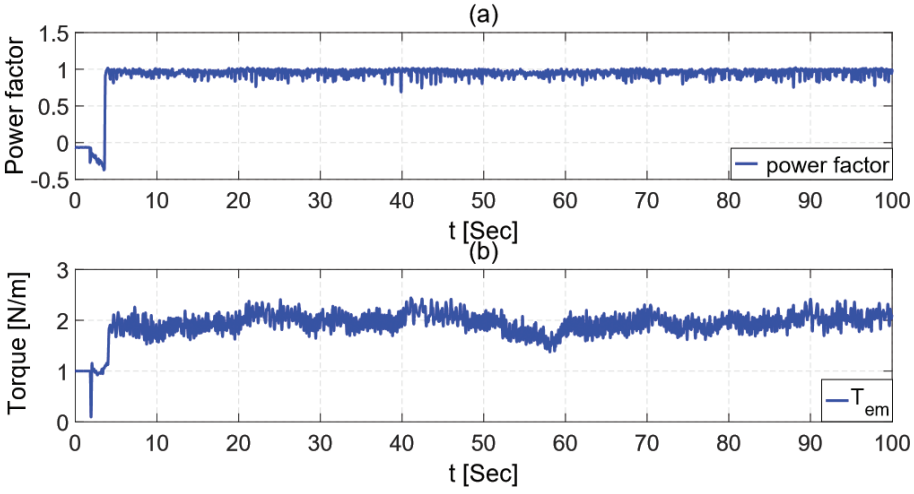

Figure 10. DFIG stator power factor and torque.

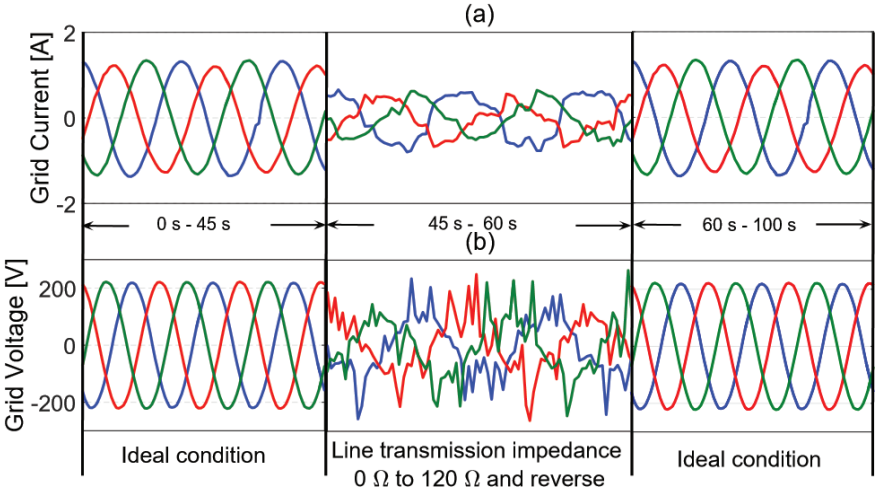

Figure 11. DFIG stator powers under grid disturbances, N-SM-L.

7.4. Fault Grid Conditions Test

In this experiment, we test that the proposed scheme ensures DFIG stability under fault grid conditions, which are caused by changing the transmission line impedance suddenly at $t = 45s$ from 0Ω to 120Ω and reversing it at $t = 60s$. Figure 11 displays the grid currents (a) and voltages (b) applied to the DFIG prototype, during the faults, at the connection point to the grid. Figure 12 illustrates the results for DFIG stator powers. The same test for SMC combined with FOC is done in [20], and the obtained results are presented in Figure 13, which illustrate that a transmission line impedance variation produces a high pick stator currents, destabilizing the system and turning-off the prototype, leading to power generation discontinuity. From this experiment's results, we conclude that the proposed control for both GSC and RSC ensures the DFIG prototype stability and rejects different disturbances, which guarantees the WT connection to the grid and ameliorates the quality and quantity of power generation. These results are achieved thanks to the adaptive control law obtained by the RHONN identifier online trained by the EKF. This configuration helps to approximate the DFIG prototype model even in the presence of disturbance. When the neural model is obtained, the feedback linearization part of the proposed control scheme is successfully able to eliminate the nonlinear part of the model including disturbances and the SM controller part can ensure the trajectory tracking with reduced value of the controller gain since the identification error is small, which helps to reduce the chattering.

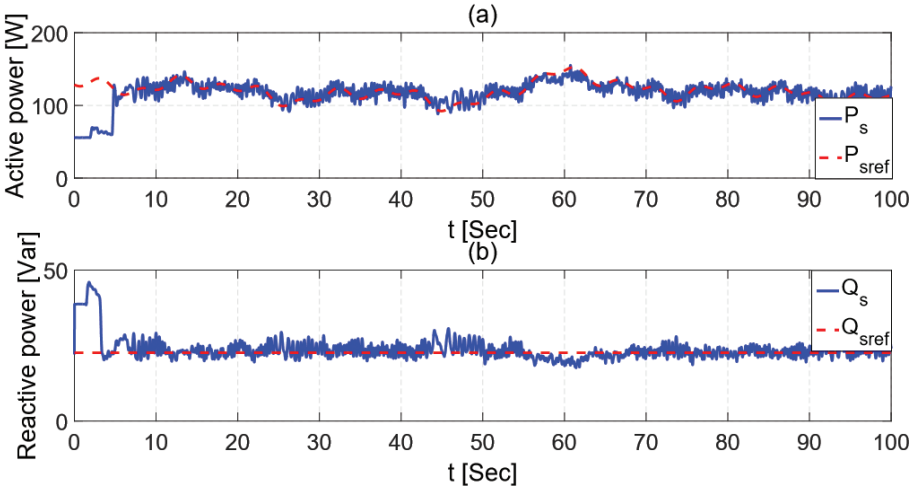

Figure 12. DFIG stator powers under grid disturbances, N-SM-L.

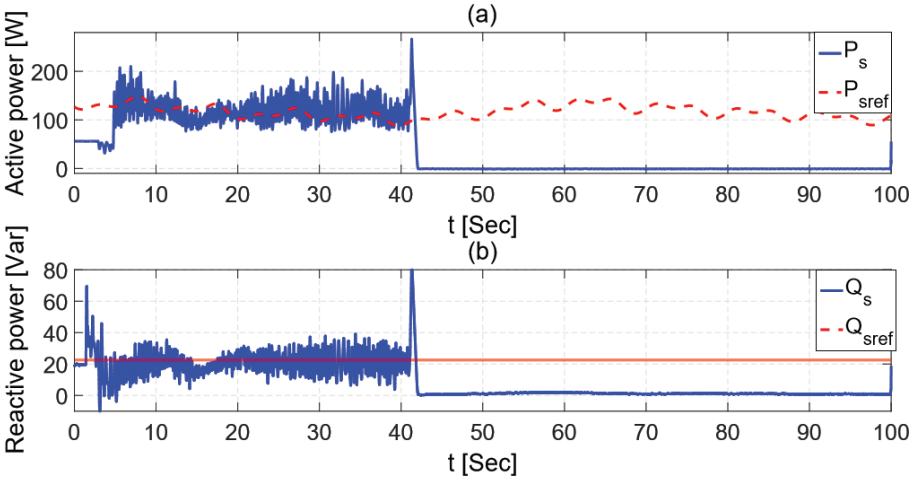

Figure 13. DFIG powers under grid disturbances, SM-FOC.

8. Conclusions

In the present paper, the development and the real-time implementation of a discrete-time N-SM-L controller is done to design a robust control scheme for a DFIG based WT. Such scheme is applied to maintain the DC voltage at a constant value, to keep at the unit value the power factor, using the GSC, and to track the DFIG generated powers desired behaviors via the rotor $d-q$ currents using the RSC. Identification is performed by RHONN identifiers for both the DFIG and the DC-link. The proposed control methodology is validated for a time-varying wind speed profile and grid disturbances. To emulate wind speeds, a DC motor is used. Experimental results validate the proposed control approach performances. Trajectory tracking is guaranteed even for time-varying desired trajectories; stability and decoupling between the control axes are also ensured. In addition, the N-SM-L controller adaptive nature offers adequate robustness in presence of DFIG prototype parameter variations and grid disturbances. Moreover, this control scheme allows maximizing the power extraction for variable wind speeds and ensures transient stability of the DFIG when a transmission line faults occur. Finally, the proposed scheme improves LVRT capacity of the DFIG and assures continuous power generation, which allows to increase generated power quantity, accomplishing modern grid codes requirements regarding LVRT capacity.

9. Appendix

Convergence Proof

Rotor Side Controller Analysis

The separation principle is applied [27] for the proposed control scheme convergence proof. Hence,

1. the identification error minimization is ensured by using the EKF to train 385 the RHONN identifier as demonstrated in [25].
2. The tracking error convergence to a small bounded region is achieved by using the proposed N-SM-L controller based on RHONN modeling as will be established in the following analysis

Due to identification error boundedness, there exists a bounded function Δ_i for the rotor currents such that

$$i_{rd,k+1} = \hat{i}_{rd,k+1} - \Delta_3 \tag{44}$$

$$i_{rq,k+1} = \hat{i}_{rq,k+1} - \Delta_4 \tag{45}$$

with $||\Delta_i|| \leq \gamma_i$, $\gamma_i > 0$, and $i = 3,4$. Substituting (23) in (44), (45) and applying the neural linearization control law (40), we obtain

$$\hat{i}_{rd,k+1} = v_{4,k} - \Delta_3 \tag{46}$$

$$\hat{i}_{rq,k+1} = v_{5,k} - \Delta_4 \tag{47}$$

The sliding surface can be rewritten for $(k + 1)$ as

$$S_{3,k+1} = \begin{bmatrix} i_{rdref,k+1} - v_{4,k} + \Delta_3 \\ i_{rqref,k+1} - v_{5,k} + \Delta_4 \end{bmatrix} \tag{48}$$

To simplify stability analysis, let define $U_k = [v_{4,k}\ v_{5,k}]^T$, $U_{eq,k} = [u_{eq4,k}\ u_{eq5,k}]^T$, $U_{n,k} = [u_{n4,k}\ u_{n5,k}]^T$, $U_0 = [u_{04}\ u_{05}]^T$, $K = [k_4\ 0;0\ k_5]$, $X_{ref,k} = [i_{rdref,k}\ i_{rqref,k}]^T$ and $\Delta = [\Delta_3\ \Delta_4]^T$,with $||\Delta|| \leq \Gamma$ and $\Gamma > 0$. The discrete-time SMC proposed in (30) and (31) includes two cases:

- Case 1:
  $||u_{c4,k}|| < u_{04}$, then $u_{c4,k}$ is used for the rotor *d* current.
  $||u_{c5,k}|| < u_{05}$, then $u_{c5,k}$ is used for the rotor *q* current.

Using (28), the sliding surface (48) is selected as

$$S_{3,k+1} = -U_{n,k} + \Delta = KS_{3,k} + \Delta \tag{49}$$

The Lyapunov function is selected as $V_k = S_{3,k}^T S_{3,k}$; its difference is calculated as

$$\begin{aligned}
\Delta V_k &= S_{3,k+1}^T S_{3,k+1} - S_{3,k}^T S_{3,k} \\
&= (KS_{3,k} + \Delta)^T (KS_{3,k} + \Delta) - S_{3,k}^T S_{3,k} \\
&\leq (\|K\|\,\|S_{3,k}\| + \|\Delta\|)^2 - \|S_{3,k}\|^2 \\
&\leq \|K\|^2\,\|S_{3,k}\|^2 + 2\,\|K\|\,\|S_{3,k}\|\,\Gamma + \Gamma^2 - \|S_{3,k}\|^2 \\
&\leq -(1 - \|K\|^2)\,\|S_{3,k}\|^2 + 2\,\|K\|\,\|S_{3,k}\|\,\Gamma + \Gamma^2 \\
&\leq -(1-\theta_1)\eta_1\,\|S_{3,k}\|^2 - \theta_1\eta_1\,\|S_{3,k}\|^2 + 2\,\|K\|\,\|S_{3,k}\|\,\Gamma + \Gamma^2 \\
&\leq -(1-\theta_1)\eta_1\,\|S_{3,k}\|^2 + \Gamma^2 + (-\theta_1\eta_1\,\|S_{3,k}\| + 2\,\|K\|\,\Gamma)\,\|S_{3,k}\|
\end{aligned}$$

with $\theta_1 < 1$ and $\theta_1 > 0$, $\eta_1 = (1 - ||K||^2)$ and $\eta_1 > 0$, and for the region $\|S_{3,k}\| \geq \frac{2\Gamma\|K\|}{\theta_1\eta_1}$, we obtain

$$\begin{aligned}
\Delta V_k &\leq -(1-\theta_1)\eta_1 \|S_{3,k}\|^2 + \Gamma^2 \\
\Delta V_k &\leq -(1-\theta_2)\beta_1 \|S_{3,k}\|^2 - \theta_2\beta \|S_{3,k}\|^2 + \Gamma^2 \\
\Delta V_k &\leq -(1-\theta_2)\beta_1 \|S_{3,k}\|^2
\end{aligned}$$

with $\theta_2 < 1$ and $\theta_2 > 0$, $\beta_1 = (1 - \theta_1)\eta_1$ and $\beta_1 > 0$. Therefore $\Delta V_k \leq 0$, $\forall \|S_{3,k}\| \geq \sqrt{\frac{\Gamma^2}{\theta_2\beta_1}}$, and the solution of the system (49) is ultimately bounded.

- Case 2:
  $||u_{c4,k}|| \geq u_{04}$, then is applied for the rotor *d* current.
  $||u_{c5,k}|| \geq u_{05}$, then is used for the rotor *q* current.

For this case, the equivalent control is selected by imposing $S_{3,k} - X_{ref,k} + X_k = 0$, with $X_{k+1} = [\hat{i}_{rd,k} \ \hat{i}_{rd,k}]^T$. Then, the equivalent control is obtained as

$$U_{eq,k} = S_{3,k} + f_k \tag{50}$$

with $f_k = -X_{ref,k} + X_k + X_{ref,k+1}$. The sliding surface is given by

$$\begin{aligned}
S_{3,k+1} &= S_{3,k} - X_{ref,k} + X_k + X_{ref,k+1} - U_k + \Delta \\
&= (S_{3,k} + f_k)(1 - U_0\frac{1}{\|U_{eq,k}\|}) + \Delta
\end{aligned}$$

Using the Lyapunov function candidate $V_k = S_{3,k}^T S_{3,k}$, then, its difference is calculated as

$$\begin{aligned}
\Delta V &\leq \left(\|S_{3,k} + f_k\| \left(1 - \|U_0\| \frac{1}{\|U_{eq,k}\|}\right) + \Delta\right)^T \\
&\quad \left(\|S_{3,k} + f_k\| \left(1 - \|U_0\| \frac{1}{\|U_{eq,k}\|}\right) + \Delta\right) - \|S_{3,k}\|^2 \\
&\leq (\|S_{3,k} + f_k\| - \|U_0\| + \|\Delta\|)^2 - \|S_{3,k}\|^2
\end{aligned}$$

Assume that the control law U_k may vary within the domain $||U_k|| \leq U_0$ [30]; considering (50) and $||\Delta|| \leq \gamma$, then $||f_k + \Delta|| \leq \sigma$ with $\sigma < ||U_0||$, so

$$\begin{aligned}
\Delta V &\leq (\|S_{3,k}\| + \sigma - \|U_0\|)^2 - \|S_{3,k}\|^2 \\
&\leq (\|S_{3,k}\| + \sigma - \|U_0\| + \|S_{3,k}\|)(\|S_{3,k}\| + \sigma - \|U_0\| - \|S_{3,k}\|) \\
&\leq (2\|S_{3,k}\| + \sigma - \|U_0\|)(\sigma - \|U_0\|) \\
&\leq -(2\|S_{3,k}\| + \sigma - \|U_0\|)(\|U_0\| - \sigma)
\end{aligned} \tag{51}$$

if $||f_k + \Delta|| \leq ||U_0|| \leq (2||S_{3,k}|| + ||f_k + \Delta||)$ holds then $\Delta V \leq 0$ [25]. Hence, the sliding manifold $||S_{3,k}||$ and the equivalent control $||U_{eq,k}||$ decrease monotonically. Therefore, it exists a time k_1 such that the equivalent control is within the domain $||U_{eq,k}|| \leq ||U_0||$ for $k \geq k_1$. At that time, the control laws u_{c4} and u_{c5} are used, yielding that the solution of system (49) is ultimately bounded. □

It is important to note that $v_{4,k}$ and $v_{5,k}$ are independent, and the convergence proof is validate for each control axis separately.

A similar analysis is valid for the Grid Side Controller, using the same procedure.

Acknowledgments

This work was supported by the Consejo Nacional de Ciencia y Tecnología (CONACyT), Mexico, under projects [257200].

References

[1] A. A. Tanvir, A. Merabet, R. Beguenane, Real-time control of active and reactive power for doubly fed induction generator based wind energy conversion system, Energies 8 (2015) 10389–10408. doi:10.3390/en80910389.

[2] Z. Elhassan, T. Y. Li, Simplified voltage control of paralleling doubly fed induction generators connected to the network using svc, International Transactions on Electrical Energy Systems 25 (11) (2015) 2847–2864. doi:10.1002/etep.1995.

[3] B. Beltran, M. E. Benbouzid, T. Ahmed-Ali, Second-order sliding mode control of a doubly fed induction generator driven wind turbine, IEEE Transactions on Energy Conversion 27 (2) (2012) 261–269. doi:10.1109/TEC.2011.2181515.

[4] V. Utkin, J. Guldner, J. Shi, Sliding mode control in Electro-Mechanical system, CRC press Taylor and Francis Group, Boca Raton, FL, 2009.

[5] R. Pena, J. Clare, G. Asher, A doubly fed induction generator using backto-back pwm converters and its application to variable-speed wind-energy generation, IEE Proceedings-Electric Power Applications 143 (3) (1996) 231–241. doi:10.1049/ip-epa:19960288.

[6] J. Morren, S. de Haan, Ride through of wind turbines with doubly-fed induction generator during a voltage dip, IEEE Transactions on Energy Conversion 20 (2) (2005) 435–441. doi:10.1109/TEC.2005.845526.

[7] V. P. Pinto, J. T. Campos, L. N. D. Reis, C. B. Jacobina, N. Rocha, Robustness and performance analysis for the linear quadratic gaussian/ loop transfer recovery with integral action controller applied to doubly fed induction generators in wind energy conversion systems, Electric Power Components and Systems journal 40 (2) (2011) 131–146. doi:10.1080/15325008.2011.629331.

[8] O. Barambones, J. A. Cortajarena, J. M. G. d. D. P. Alkorta, Real-time sliding mode control for a wind energy system based on a doubly fed induction generator, Energies 7 (2014) 6412–6433. doi:10.3390/en7106412.

[9] E. Sanchez, R. Riemann, Doubly Fed Induction Generators: Control for Wind Energy, CRC press Taylor and Francis Group, Boca Raton, FL, 2016.

[10] R. K. Patnaik, P. K. Dash, K. Mahapatra, Adaptive terminal sliding mode power control of dfig based wind energy conversion system for stability enhancement, International Transactions on Electrical Energy Systems 26 (4) (2016) 750–782. doi:10.1002/etep.2105.

[11] M. Ezzat, M. Benbouzid, S. Muyeen, L. Harnefors, Low-voltage ridethrough techniques for dfig-based wind turbines: state-of-the-art review and future trends, in: 39 th Annual Conference of the IEEE Industrial Electronics Society, Vienna, Austria, 2013, pp. 7681–7686. doi: 10.1109/IECON.2013.6700413.

[12] I. Sadeghkhani, M. E. Golshan, A. Mehrizi-Sani, J. M. Guerrero, Lowvoltage ride-through of a droop-based three-phase four-wire grid-connected microgird, IET Generation, Transmission & Distribution 12 (8) (2018) 1906–1914. doi:10.1049/iet-gtd.2017.1306.

[13] N. Y. Abed, M. M. Kabsha, G. M. AbdIsalam, Low voltage ride-through protection techniques for dfig wind generator, in: 2013 IEEE Power & Energy Society General Meeting, Vancouver, BC, Canada, 2013. doi:10.1109/PESGM.2012.6345594.

[14] L. Yang, Z. Xu, J. Ostergaard, Z. Dong, K. Wong, Advanced control strategy of dfig wind turbines for power system fault ride through, IEEE Transactions on Power Systems 27 (2012) 713–722. doi:10.1109/TPWRS.2011.2174387.

[15] J. J.Justo, R.C.Bansal, Parallel r-l configuration crowbar with series r-l circuit protection for lvrt strategy of dfig under transient-state, Electric Power System Research 154 (2018) 299–310. doi:10.1016/j.epsr.2017. 09.002.

[16] J. J.Justo, F.Mwasilu, J. W. Jung, Enhanced crowbarless frt strategy for dfig based wind turbines under three-phase voltage dip, Electric Power System Research 142 (2017) 215–226. doi:10.1016/j.epsr.2016.09.029.

[17] Y. Zhou, P. Bauer, J. Ferreira, J. Pierik, Operation of grid-connected dfig under unbalanced grid voltage condition, IEEE Transactions on Energy Conversion 24 (1) (2009) 240–246. doi:10.1109/TEC.2008.2011833.

[18] J. Hu, Y. He, L. Xu, B. Williams, Improved control of dfig systems during network unbalance using pi-r current regulators, IEEE Transactions on Industrial Electronics 56 (2) (2009) 439–451. doi:10.1109/TIE.2008.2006952.

[19] M. J. Morshed, A. Fekih, A new fault ride-through control for dfig-based wind energy systems, Electric Power System Research 146 (2017) 258–269. doi:10.1016/j.epsr.2017.02.010.

[20] L. Djilali, E. N. Sanches, M. Belkheiri, Real time implementation of sliding mode field oriented control for a dfig based wind turbine, International Transactions on Electrical Energy Systems 28 (5) (2018) 1–26. doi:10.1002/etep.2539.

[21] M. Martinez, G. Tapia, A. Susperregui, H. Camblong, Sliding-mode control 505 of a wind turbine-driven double-fed induction generator under non-ideal grid voltages, IET Renewable Power Generation 7 (4) (2013) 370–379. doi:10.1049/iet-rpg.2012.0172.

[22] D. Sun, X. Wang, H. Nian, Z. Q. Zhu, A sliding-mode direct power control strategy for dfig under both balanced and unbalanced grid conditions using extended active power, IEEE Transactions on Power Electronics 33 (2018) 1313–1322. doi:10.1109/TPEL.2017.2686980.

[23] R. Ruiz-Cruz, E. N. Sanchez, A. Loukianov, J. A. Ruz-Hernandez, Realtime neural inverse optimal control for a wind generator, IEEE Transactions on Sustainable Energy (Early Access) 10 (3) (2019) 1172–1183. doi:10.1109/TSTE.2018.2862628.

[24] L. Djilali, E. N. Sanches, M. Belkheiri, Real-time neural sliding mode field oriented control for a dfig-based wind turbine under balanced and unbalanced grid conditions, IET Renewable Power Generation 13 (4) (2019) 618–632. doi:10.1049/iet-rpg.2018.5002.

[25] E. N. Sanchez, A. Y. Alanis, A. G. Loukianov, Discrete-Time High Order Neural Control trained with Kalman filtering, Springer Science & Business Media, Verlag London, Uk, 2008.

[26] G. Rovithakis, M. Chistodoulou, Adaptive Control with Recurrent High Order Neural Networks, Springer Science & Business Media, Verlag London, UK, 2012.

[27] W. Lin, C. I. Byrnes, Design of discrete-time nonlinear control systems via smooth feedback, IEEE Transactions on Automatic Control 39 (11) (1994) 2340–2346. doi:10.1109/9.333790.

[28] L. Saihi, B. Berbaoui, H. Glaoui, L. Djilali, S. Abdeldjalil, Robust sliding 530 mode h_{∞} controller of dfig based on variable speed wind energy conversion system, Periodica Polytechnica Electrical Engineering and Computer Science 64 (2020) 53–63. doi:doi.org/10.3311/PPee.14490.

[29] J. Hu, Y. He, L. Xu, B. Williams, Four-quadrant dynamometer/power supply, Festo LabVolt Datasheet.

[30] G. Bartolini, A. Ferrara, V. I. Utkin, Adaptive sliding mode control discrete-time system, Automatica 31 (5) (1995) 769–773.